



Analysis of RC Continuous Beams Strengthened with FRP Plates: A Finite Element Model

Mohammed A. Sakr ^{a*}, Tarek M.Khalifa ^b, Walid N.Mansour ^c

^a Assoc. Prof., Department of Structural Engineering, Tanta University, Tanta, Egypt.

^b Assis. Prof., Department of Structural Engineering, Tanta University, Tanta, Egypt.

^c Assistant lecturer, Department of Civil Engineering, Kafrelsheikh University, Kafrelsheikh, Egypt.

Received 21 October 2016; Accepted 25 November 2016

Abstract

Strengthening of reinforced concrete (RC) beams with externally bonded fibre reinforced polymer (FRP) plates/sheets technique has become widespread in the last two decades. Although a great deal of research has been conducted on simply supported RC beams, a few studies have been carried out on continuous beams strengthened with FRP composites. This paper presents a simple uniaxial nonlinear finite-element model (UNFEM) that is able to accurately estimate the load-carrying capacity and the behaviour of RC continuous beams flexurally strengthened with externally bonded FRP plates on both of the upper and lower fibres. A 21-degree of freedom element is proposed with layer-discretization of the cross-sections for finite element (FE) modelling. Realistic nonlinear constitutive relations are employed to describe the stress-strain behaviour of each component of the strengthened beam. The FE model is based on nonlinear fracture mechanics. The interfacial shear and normal stresses in the adhesive layer are presented using an analytical uncoupled cohesive zone model with a mixed-mode fracture criterion. The results of the proposed FE model are verified by comparison with various selected experimental measurements available in the literature. The numerical results of the plated beams (beams strengthened with FRP plates) agreed very well with the experimental results. The use of FRP increased the ultimate load capacity up to 100 % compared with the non-strengthened beams as occurred in series (S). The major objective of the current model is to help engineers' model FRP-strengthened RC continuous beams in a simple manner.

Keywords: Finite Element; Continuous Beams; Plated Beam; Interfacial Stresses; Maximum Capacity; Debonding.

1. Introduction

In recent years, the external bonding of carbon (CFRP) or glass (GFRP) FRP plates/sheets to the beam tension face has become a common practice and is widely used to strengthen or repair structures. Strengthening RC beams in flexure with FRP plates/sheets is a powerful strengthening technique due to its simplicity of in situ application, small increase of the beam size and weight, and good resistance to corrosion.

Extensive numerical and experimental research efforts have been carried out to study and model the behavior of simply supported beams with external FRP plates; as a result, there are many design guidelines for such beams [1-3]. However, many in situ RC beams are used in continuous construction; there has been very limited research into the behavior of such beams with external strengthening. Experimental studies were conducted to compare the behavior of RC continuous beams strengthened with FRP plates with non-strengthened beams (control beams) [4-15]. They concluded that the use of FRP plates/sheets to strengthen continuous beams was effective for reducing deflections and for increasing their load carrying capacity.

* Corresponding author: mhsakr010@yahoo.com

Subhashree [16] tested fourteen symmetrical continuous (two-span) beams. The beams were grouped into two series. Each series had a different percentage of steel reinforcement. One beam from each series was not strengthened and was considered a control beam, whereas all other beams were strengthened in various patterns with externally bonded GFRP sheets. The study concluded that the beam that was strengthened by U-wrap and anchored using a steel plate and bolt system; showed the highest ultimate load. The percentage increase of the load capacity of that beam was 61.92%. The load carrying capacity of the beam that was strengthened by four layers of U-wrap in the positive moment zone had near the load capacity of the beam strengthened by two layers of U-wrap and anchored using the steel plate and bolt system. The percentage increase of the load carrying capacity of that beam was 59.61 %. The use of a steel bolt and plate system is an effective method of anchoring the FRP sheet to prevent the debonding failure. Strengthening the continuous beam by providing a U-wrap of an FRP sheet is also an effective way of enhancing the load carrying capacity.

Previous FE studies of FRP-strengthened beams involved the use of refined FE meshes of two-dimensional plate/shell elements [17-20] or three-dimensional solid elements [21] using many commercial FE packages. Using the commercial numerical FE package Abaqus, Obaidat et al. [22]; suggested a 3D FE model to analyze plate end interfacial debonding in retrofitted RC beams. A nonlinear cohesive bond model under mode-II conditions was used for the concrete-FRP interface. The computational cost of structural response analyses based on FE models, such as the ones referred to above, is very high.

Barbato [23] proposed a force-based frame FE to estimate the load carrying capacity of simply supported RC beams strengthened with externally bonded FRP strips and plates. In this model, the bond between the RC beam and FRP plate is considered using an appropriate modification of a constitutive model representing FRP. The uniaxial model of [23] has a very low computational cost compared with the above 2D or 3D models constructed using FE-packages.

Although many research studies have been carried out to understand and model debonding failure modes, it is still a very active field of research, mainly due to the complexity of the problem at hand. After thoroughly searching the literature, the authors found that there are no analytical solution models of the non-linear mode-I and mode-II fracture responses of the cohesive interface of strengthened RC beams with FRP plates or strips. Here, the importance of the current work appears.

The research work presented in this paper develops a new uniaxial nonlinear finite-element model that is able to simulate the mechanical behavior of FRP-strengthened RC continuous beams utilizing realistic nonlinear constitutive relations for each strengthened beam component. The interfacial shear and normal stresses in the adhesive layer are presented using an analytical uncoupled cohesive zone (CZ) model based on nonlinear fracture mechanics. This model introduces accurate predictions for the ultimate load of FRP-strengthened RC continuous beams and; a sound mechanical description and interpretation for failure modes, the innovation of this UNFEM is to reduce the complexity of FE analyses based on existing 2D or 3D FE models constructed using FE packages; and simulates the structural response of the considered beams.

2. Finite Element Modeling

As shown in Figure 1. there are three components in a strengthened beam for the present analysis model, i.e., reinforced concrete, FRP and adhesive.



Figure 1. RC beam bonded with an FRP plate

The adhesive layer is modeled to handle cohesive forces in both the normal and tangential directions. The interfacial shear and normal stresses in the adhesive layers or in the CZ are shown in Figure 2.

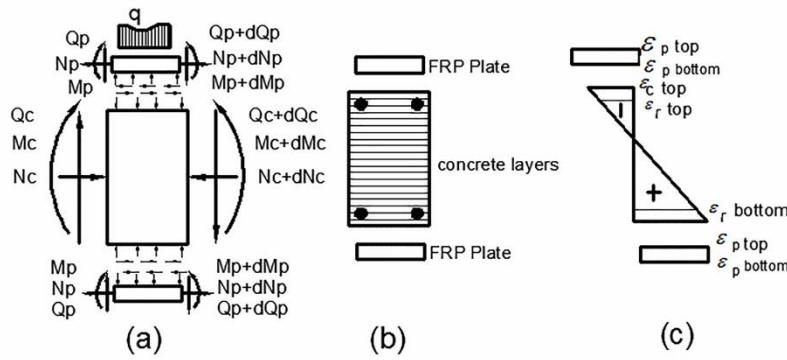


Figure 2. (a) Differential element along the span; (b) general cross section geometry and layer discretization; and (c) strain distribution [24]

A 21-degree of freedom element is developed to represent the strengthened RC beam. The 21 degrees of freedom are: (1) seven degrees of freedom represent the horizontal slippage, the vertical separation, and the rotation of the upper FRP plate (2) seven degrees of freedom represent the horizontal slippage, the vertical separation, and the rotation of the lower FRP plate (3) seven degrees of freedom represent the horizontal displacement, the vertical displacement, and the rotation of the concrete, as shown in Figure 3. The RC beam and FRP layer are modeled as beams with Euler-Bernoulli kinematics assumptions. Linear geometry, due to small deformations and displacements, is assumed. The CZ model is utilized for determining the normal and tangential stiffness of the adhesive layer. A perfect bond is assumed between the concrete and reinforcing steel.

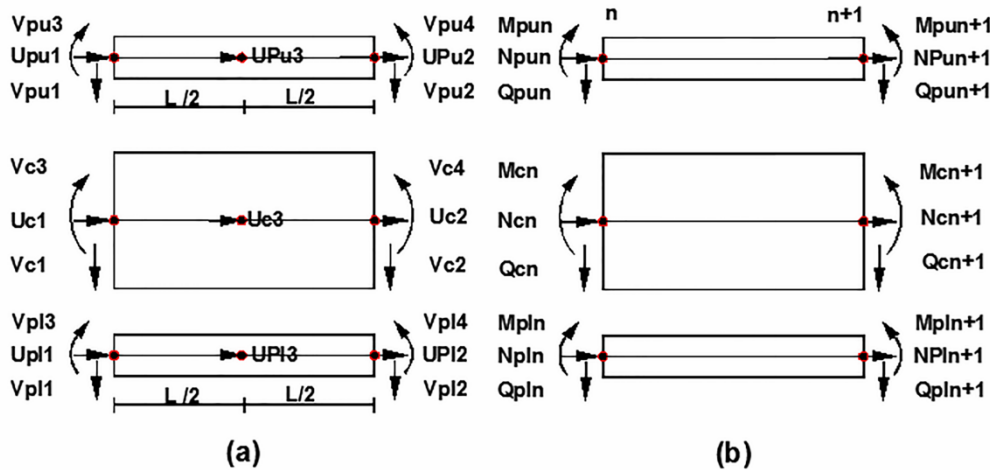


Figure 3. (a) The developed finite element: (a) nodal degrees of freedom; (b) nodal forces

2.1. Constitutive Equations of Materials

A layered model approach was followed during the development of the proposed FE for the concrete beam cross section. The cross section was divided into a finite number of layers, as shown in Figure 2. The layered model approach is relevant for the formulation of these types of complex elements due to the difference between the properties of beam reinforcement and concrete and the dissimilarity between the behavior of concrete in tension and compression. For concrete in compression, the stress-strain relationship suggested by [25] is adopted. This relationship is characterized by linear-elastic behavior up to 40% of the maximum strength f_c . Beyond the elastic limit, an elastic-plastic with final softening branch is assumed (Figure 4a). For concrete in tension, linear-elastic behavior is considered up to the cracking phenomenon, which occurs when the tensile strength f_{ct} is reached. The tension stiffness of concrete between cracks, due to the presence of reinforcement, is taken into account by the nonlinear softening law proposed by [26] and modified by [27] to take into account the size effect. Compared to the case of concrete without reinforcement, the tensile stress does not vanish for large strain, but it tends to a positive value that depends on the percentage of reinforcement in the concrete beam. For reinforcement steel, an elastic-plastic with small hardening law typically used for structural steel has been assumed (Figure 4b). In Figure 4b, f_y and ϵ_y are the yield strength and strain, while f_u and ϵ_u are the ultimate strength and strain. The FRP is modeled with linear elastic-brittle behavior in tension and zero-strength and stiffness in compression (Figure 4c). f_{pu} and ϵ_{pu} , shown in Figure 4c, are the ultimate tensile strength and strain.

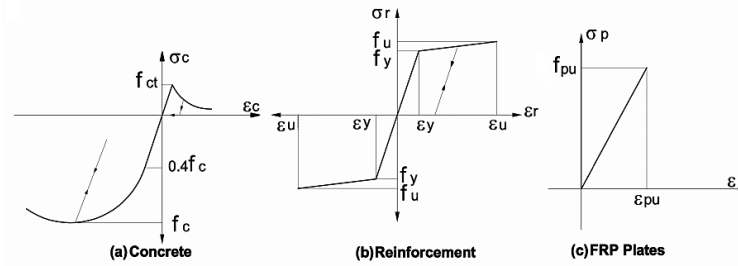


Figure 4. The adopted stress-strain relationships

Due to its simplicity, CZ modeling is largely used for the behavior of adhesive layers. The energy release rates in mode-I (GI) and mode-II (GII) are identified as the areas under the respective cohesive laws integrated up to the current values of stresses. The total energy release rate is the sum of GI and GII. Different approaches have been used in the literature for CZ modeling of interfaces under mixed-mode conditions:

In the uncoupled CZ approach, cohesive laws in the normal and tangential directions are independent of each other. Fracture is assumed to occur when the energy release rate equals the fracture energy of the adhesive (the total area under the descending part of the load-displacement curves). If the mixed-mode fracture criterion of the adhesive layer is known, the strength of the joint can be predicted by equating the energy-release rate to the fracture energy. The simplest possible mixed-mode fracture criterion is:

$$\frac{G_I}{G_{If}} + \frac{G_{II}}{G_{IIf}} = 1 \tag{1}$$

Where G_{If} and G_{IIf} denote, respectively, the fracture energies in pure mode-I and mode-II conditions. This approach was used by [28] and [29]. They suggested that, once the failure condition is reached, the element is considered no longer capable of bearing any load.

In the coupled CZ approach, cohesive laws in the normal and tangential directions are linked to each other, typically by means of a coupling parameter. Tvergaard [30] developed a coupled cohesive law derived from a potential using a dimensionless coupling parameter between the normal and tangential laws. With this approach, the fracture energy is the same in all mode mixities. This is often regarded as a drawback, as the experimental evidence indicates that the fracture energy is often significantly larger in mode-II than in mode-I [31].

In the current study, uncoupled cohesive laws are considered both in the normal and tangential directions. Tension relates the normal relative displacement, $g^N > 0$, and the normal stress, p^N , while shear relates the tangential relative displacement, g^T , and the tangential stress, p^T . This choice is made to help in using different values for the mode-I and mode-II interfacial fracture energies, in agreement with the experimental evidence. The cohesive laws implemented herein are bilinear (Figure 5).

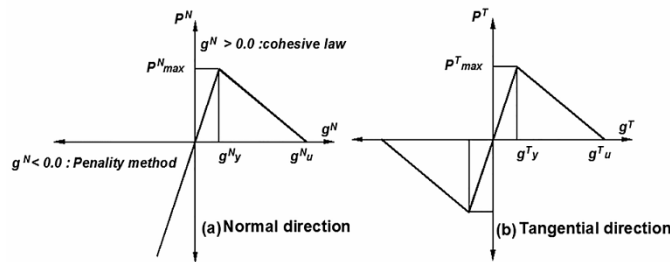


Figure 5. Relationship between interfacial tractions and relative displacements

This simple shape is able to capture the three characteristic parameters of the interface, i.e., the fracture energies (the areas underneath the curves), the cohesive strengths, p^N_{max} and p^T_{max} , and the linear-elastic properties (the slopes of the curves in the ascending branch, K^T and K^N , which are defined below [32]).

$$K^N = \frac{1}{\frac{t_a}{E_a} + \frac{t_c}{E_c}} \quad K^T = \frac{1}{\frac{t_a}{G_a} + \frac{t_c}{G_c}} \tag{2}$$

t_a is the adhesive layer thickness; t_c is the concrete cover thickness; E_c and E_a are the modulus of the elasticity of

concrete and adhesive, respectively, and G_c and G_a are the shear modulus of concrete and adhesive, respectively. The specific mode I fracture energy G_{If} can be deduced from the load-displacement curve or the value given in the [2]. The specific mode II fracture energy G_{IIIf} was considered in the manner conducted by [19]. The cohesive tensile strength p^Nmax was taken to be the concrete tensile strength, while the cohesive tangential strength p^Tmax value was taken from an equation derived by [19]. Following the approach given by [28] the energy release rates in mode-I and mode-II are identified as the areas under the respective cohesive laws integrated up to the current values of g^N and g^T , and the simplest possible mixed-mode failure criterion is assumed, as in Eq. (1). The mode-mixities can be estimated directly from the numerical predictions by examining the value of G_{II}/G_I for a crack-tip CZ element just before it fails. The above cohesive models have been implemented in a 21-node composite element proposed by the current study, and generalized to handle cohesive forces in both the normal and tangential directions. Additionally, all the above constitutive equations of materials for concrete in tension or compression, reinforcement, and FRP have been implemented in that element.

2.2. Element Formulation

With reference to the parameters of the nodal displacements of the element shown in Figure 3, the following relationships can be written:

$$\begin{aligned}
 u_{pl}(x) &= \mathbf{N}_p \cdot \mathbf{U}_{pl}; \quad u_{pu}(x) = \mathbf{N}_p \cdot \mathbf{U}_{pu}; \quad u_c(x) = \mathbf{N}_c \cdot \mathbf{U}_c; \quad v_{pl}(x) = \mathbf{N}_{vp} \cdot \mathbf{V}_{pl}; \quad v_{pu}(x) = \mathbf{N}_{vp} \cdot \mathbf{V}_{pu}; \\
 v_c(x) &= \mathbf{N}_{vc} \cdot \mathbf{V}_c
 \end{aligned}
 \tag{3}$$

where c , pl , and pu are subscripts relating the symbol to the centroid of the reinforced concrete beam and the centroid of the lower and upper FRP plates, respectively; $\mathbf{U}^T = [u_1, u_2, u_3]$ is the vector of the nodal horizontal displacements, and $\mathbf{N} = [N_1(x), N_2(x), N_3(x)]$ is the vector of the corresponding shape functions. Analogously, \mathbf{V} is the vector of the vertical nodal displacement, and \mathbf{N}_v is the vector of the corresponding shape functions. The tangent displacement (horizontal slip) $g^T(x)$ and normal displacement (vertical separation) $g^N(x)$ can be written as:

(i) Lower part:

$$g_i^T(x) = -\mathbf{N}_c \cdot \mathbf{U}_c + \mathbf{N}_p \cdot \mathbf{U}_{pl} + (H/2)\mathbf{N}'_{vc} \cdot \mathbf{V}_c + (t_{pl}/2)\mathbf{N}'_{vp} \cdot \mathbf{V}_{pl} \tag{4}$$

$$g_i^N(x) = -\mathbf{N}_{vc} \cdot \mathbf{V}_c + \mathbf{N}_{vp} \cdot \mathbf{V}_{pl} \tag{5}$$

(ii) Upper part:

$$g_u^T(x) = \mathbf{N}_c \cdot \mathbf{U}_c - \mathbf{N}_p \cdot \mathbf{U}_{pu} + (H/2)\mathbf{N}'_{vc} \cdot \mathbf{V}_c + (t_{pu}/2)\mathbf{N}'_{vp} \cdot \mathbf{V}_{pu} \tag{6}$$

$$g_u^N(x) = \mathbf{N}_{vc} \cdot \mathbf{V}_c - \mathbf{N}_{vp} \cdot \mathbf{V}_{pu} \tag{7}$$

Where \mathbf{N}'_{vc} and \mathbf{N}'_{vp} are the first derivatives of the matrices \mathbf{N}_{vc} and \mathbf{N}_{vp} , respectively. The strain $\epsilon_{ci}(x)$ of the i^{th} concrete layer can be expressed as a function of the element nodal displacements as follows:

$$\epsilon_{ci}(x) = \mathbf{N}'_c \cdot \mathbf{U}_c + y_i \mathbf{N}''_{vc} \cdot \mathbf{V}_c \tag{8}$$

where \mathbf{N}'_c is the first derivative of the matrix \mathbf{N}_c , \mathbf{N}''_{vc} is the second derivative of the matrix \mathbf{N}_{vc} , and y_i is the distance from the middle of the reinforced concrete beam to the centroid of the i^{th} concrete layer. In a similar manner, the strains of the reinforcement steel layers and FRP plate are given as follows:

$$\epsilon_r(x) = \mathbf{N}'_c \cdot \mathbf{U}_c + y_r \mathbf{N}''_{vc} \cdot \mathbf{V}_c \tag{9}$$

$$\epsilon_{pl}(x) = \mathbf{N}'_p \cdot \mathbf{U}_{pl} + y_{pl} \mathbf{N}''_{vp} \cdot \mathbf{V}_{pl} \tag{10}$$

$$\epsilon_{pu}(x) = \mathbf{N}'_p \cdot \mathbf{U}_{pu} + y_{pu} \mathbf{N}''_{vp} \cdot \mathbf{V}_{pu} \tag{11}$$

where \mathbf{N}'_p is the first derivative of the matrix \mathbf{N}_p , \mathbf{N}''_{vp} is the second derivative of the matrix \mathbf{N}_{vp} , y_r is distance between the centroid of the reinforcement bars to the middle surface of the reinforced concrete beam, and; y_{pl} and y_{pu} are the distances measured from the centroid of the lower and upper FRP plates to the point at which the strain is calculated, respectively. The studied problem is nonlinear and can be solved through iterations. Applying the principle of virtual work to a certain element for a specific iteration j , the system of six equations can immediately be obtained and written in matrix form;

$$K_k^j U_k^j = f_k^j \quad (12)$$

Where K_k^j represents the stiffness matrix of the generic element, U_k^j is the unknown nodal displacement vector of the element, and f_k^j is the load (known values) vector.

Once the system of Equation 12. has been obtained, one can rearrange the equations and carry out a static condensation procedure of the equations of the internal nodal parameters, and to obtain a reduced system. For a generic beam made up of several elements, using the usual technique of the finite element method for assembling, applying the boundary condition, and adding the nodal forces to the load vector at the conventional position, the system of linear algebraic equations can be obtained in the following form:

$$K^j \cdot U^j = F^j \quad (13)$$

Where K^j and U^j are the stiffness matrix, the vector of unknown nodal displacements, and the load vector including all nodal forces, respectively, for iteration j .

The discretization of elements is not uniform. Thus, a fine mesh consisting of elements with different lengths is used. Elements where the stresses varied strongly, e.g., at the end of FRP plates, at the intermediate support and at the positions of concentrated loads, are relatively small with lengths in the range (0.2 to 0.5 cm), while the lengths of the other elements range from 1 to 5 cm. These values are recommended based on many solved examples, which showed that using finer meshes does not yield significant differences in results. The small lengths of elements facilitate and improve the convergence.

2.3. Solution Algorithm and Convergence

To solve the nonlinear response of the strengthened RC continuous beam with FRP plates, the secant method is adopted to determine the unknown deformations, considering the origin point as a base point for all secant models. The secant method is relevant for implementation in the proposed FE model because the secant modulus is always positive, something that facilitates convergence of the solution. The total nodal deformations, not the incremental deformations, are the independent variables of each iteration. Utilizing the total nodal deformations and material constitutive laws in total form is straightforward and makes it easy to consider time history analysis in a total form at a specific time.

2.4. Plate end Debonding Failure Modes

At the plate end, the beam can fail by two different modes, either by interfacial debonding of FRP or concrete cover separation due to a combination of interfacial shear and normal stresses concentrating near the plate end. Plate end failure is a complex phenomenon. The failure starts at the end of the FRP plate and propagates towards mid-span along a plane just above the adhesive layer between the RC beam and FRP (mode A) or along a plane immediately below the reinforcing steel bars (concrete cover separation - mode B). Thus, two different models (Model A and B) were developed in the proposed uniaxial nonlinear finite-element model. In Model A, the CZ plane is inserted just above the adhesive layer, while in Model B, the CZ is inserted immediately below the reinforcing steel, and the concrete cover and FRP plates are considered a composite beam with a perfect bond. In model B, the cohesive zone parameters are considered a tensile and shear strength, modulus of elasticity and rigidity, and tensile and shear fracture energies of concrete multiplied by the width of the RC beam. Effective stiffness factors for that composite beam were calculated depending on the nonlinear stress-strain relationship of concrete layers and FRP plates. The analysis using either Model A or Model B shows the same results for deformation and stresses until the initiation of the first crack at the plate end. For each RC continuous beam, analysis using the two different models should be conducted. The expected failure mode (A) or (B) and ultimate load of the beams with plate end failure is the premature (minimum) one of either Model A or Model B.

3. Numerical Validation

3.1. Prediction of the Ultimate Load-Carrying Capacity

The proposed FE model is evaluated through a comparison between the experimentally measured and the numerically predicted load-carrying capacity of the beams included in the experimental database. Table 1. and Table 2. provide the geometric properties of the specimens shown in Figure 6. and the most important mechanical properties of the used materials, including both reference (i.e., non-strengthened) and FRP-strengthened beams. Geometric properties of the specimens and mechanical properties of the materials are taken from the test data and available experimental information provided in the referred literature [7, 16] and mostly obtained through steel coupon and FRP tensile tests or concrete compression tests.

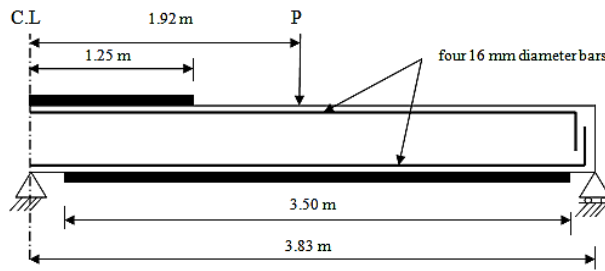


Figure 6. Geometric properties of the specimens tested in [7]

The specific mode I fracture energy G_{If} was considered to be 70 N/m, as recommended by the CEB-FIB Model code in [2] and [19]. The specific mode II fracture energy G_{IIIf} was considered to be 200 N/m, as done by [19]. The cohesive tangential strength value, 3.0 MPa, was taken from the equation derived by [19].

Table 3. and Table 4. show a comparison between the experimental ultimate load capacity; P_{exp} , ultimate negative bending moment; M_{exp}^- , and ultimate positive bending moment M_{exp}^+ at the failure of the test specimens and a comparison between the predicted FE ultimate load capacity P_{FE} , ultimate negative bending moment; M_{FE}^- , and ultimate positive bending moment M_{FE}^+ obtained by the uniaxial nonlinear finite-element model at the failure of the test specimens.

The ratio between the predicted and the experimental values ranges from 0.93 to 1.17, 0.84 to 1.18, and 0.83 to 1.16 for the ultimate load capacity, ultimate negative bending moment, and ultimate positive bending moment, respectively. The agreement between the experimental results and the predicted results is good for both the reference beams and the strengthened beams.

Table 1. Experimental test database: geometry and material properties of the RC beam specimens

| Authors | ID | Span (mm) | Width (mm) | Height (mm) | A_{stop} (mm ²) | $A_{s\ bottom}$ (mm ²) | f_c (MPa) | f_y (MPa) | E_y (GPa) |
|-------------------|-----------------|-----------|------------|-------------|-------------------------------|------------------------------------|-------------|-------------|-------------|
| Ashour et al. [7] | H ₁ | 3830 | 150 | 250 | 100.5 | 628.3 | 24.0 | 510 | 200 |
| | H ₂ | | | | 100.5 | 628.3 | 43.5 | 510 | 200 |
| | H ₃ | | | | 100.5 | 628.3 | 33.0 | 510 | 200 |
| | H ₄ | | | | 100.5 | 628.3 | 33.2 | 510 | 200 |
| | H ₅ | | | | 100.5 | 628.3 | 46.0 | 510 | 200 |
| | H ₆ | 100.5 | 628.3 | 44.0 | 510 | 200 | | | |
| | S ₁ | 2000 | 150 | 200 | 628.3 | 100.5 | 26.0 | 505 | 200 |
| | S ₂ | | | | 628.3 | 100.5 | 42.9 | 505 | 200 |
| | S ₃ | | | | 628.3 | 100.5 | 33.3 | 505 | 200 |
| | S ₄ | | | | 628.3 | 100.5 | 42.8 | 505 | 200 |
| | S ₅ | | | | 628.3 | 100.5 | 24.4 | 505 | 200 |
| | E ₁ | | | | 402.1 | 402.1 | 24.0 | 520 | 201 |
| | E ₂ | | | | 402.1 | 402.1 | 43.6 | 520 | 201 |
| | E ₃ | | | | 402.1 | 402.1 | 47.8 | 520 | 201 |
| | E ₄ | | | | 402.1 | 402.1 | 46.1 | 520 | 201 |
| E ₅ | 402.1 | | | | 402.1 | 44.7 | 520 | 201 | |
| Subhashree [16] | CB ₁ | | | | 226.2+157.08* | 100.53 | 22.67 | 578 | 200 |
| | CB ₂ | 2000 | 150 | 200 | 56.55+157.08* | 157.08 | 25.34 | 429 | 200 |
| | SB1 | | | | 226.2+157.08* | 100.53 | 23.3 | 578 | 200 |
| | TB1 | | | | 56.55+157.08* | 157.08 | 24.5 | 429 | 200 |

*provided at the top tension zone

$A_{s\ top}$ = Area of the top steel

$A_{s\ bottom}$ = Area of the bottom steel

E_y = Elastic modulus of the reinforcement bars

Table. 2 Experimental test databases: geometry and material properties of the FRP reinforcement for the FRP-strengthened RC beams

| Authors | ID | Material | Top FRP over the central support | | Bottom FRP at mid span | | b_f (mm) | f_{pu} (MPa) | E_r (GPa) |
|-------------------|-----------------|-------------|----------------------------------|------------|------------------------|------------|------------|----------------|-------------|
| | | | t_f (mm) | L_1 (mm) | t_f (mm) | L_2 (mm) | | | |
| Ashour et al. [7] | H ₂ | CFRP sheets | 0.234 | 2000 | - | - | 110 | 3900 | 240 |
| | H ₃ | CFRP sheets | 0.702 | 2000 | - | - | 110 | 3900 | 240 |
| | H ₄ | CFRP sheets | 1.17 | 2000 | - | - | 110 | 3900 | 240 |
| | H ₅ | CFRP sheets | 0.702 | 1000 | - | - | 110 | 3900 | 240 |
| | H ₆ | CFRP sheets | 0.234 | 3000 | 0.234 | 1000 | 110 | 3900 | 240 |
| | S ₂ | CFRP sheets | - | - | 0.234 | 2000 | 110 | 3900 | 240 |
| | S ₃ | CFRP sheets | - | - | 0.702 | 2000 | 110 | 3900 | 240 |
| | S ₄ | CFRP sheets | - | - | 0.702 | 3500 | 110 | 3900 | 240 |
| | S ₅ | CFRP sheets | - | - | 1.17 | 3500 | 110 | 3900 | 240 |
| | E ₂ | CFRP plate | 1.2 | 2500 | - | - | 100 | 2500 | 150 |
| | E ₃ | CFRP plate | - | - | 1.2 | 3500 | 100 | 2500 | 150 |
| | E ₄ | CFRP plate | 1.2 | 2500 | 1.2 | 3500 | 100 | 2500 | 150 |
| | E ₅ | CFRP sheets | .702 | 2500 | - | - | 110 | 3900 | 240 |
| Subhashree [16] | SB ₁ | GFRP plate | 3.0 | 880 | 1.0 | 880 | 150 | 172.79 | 6.829 |
| | TB ₁ | GFRP plate | 3.0 | 880 | 1.0 | 880 | 150 | 172.79 | 6.829 |

Table 3. Comparison between the experimental results and numerical results of the load-carrying capacity of the reference RC beams (i.e., without FRP reinforcement)

| Authors | ID | P_{exp} (kN) | P_{FE} (kN) | $\frac{P_{FE}}{P_{exp}}$ | M_{exp}^- (kN.m) | M_{FE}^- (kNm) | $\frac{M_{FE}^-}{M_{exp}^-}$ | M_{exp}^+ (kN.m) | M_{FE}^+ (kN.m) | $\frac{M_{FE}^+}{M_{exp}^+}$ | Failure mode |
|-------------------|-----------------|----------------|---------------|--------------------------|--------------------|------------------|------------------------------|--------------------|-------------------|------------------------------|--------------|
| Ashour et al. [7] | H ₁ | 138 | 137.2 | 0.99 | 21.21 | 23.89 | 1.12 | 56.78 | 53.73 | 0.95 | Flexure |
| | S ₁ | 83.6 | 86.20 | 1.03 | 57.77 | 55.00 | 0.95 | 11.13 | 13.77 | 1.23 | Flexure |
| | E ₁ | 149.7 | 148.2 | 0.99 | 54.49 | 48.95 | 0.90 | 44.41 | 46.47 | 1.04 | Flexure |
| Subhashree [16] | CB ₁ | 260 | 256.2 | 0.99 | - | 29.24 | - | - | 17.41 | - | Flexure |
| | CB ₂ | 200 | 194.2 | 0.97 | - | 13.39 | - | - | 17.58 | - | Flexure |

Table 4. Comparison between the experimental results and numerical results of the load-carrying capacity of the FRP-strengthened RC beams

| Authors | ID | P_{exp} (kN) | P_{FE} (kN) | $\frac{P_{FE}}{P_{exp}}$ | M_{exp}^- (kN.m) | M_{FE}^- (kNm) | $\frac{M_{FE}^-}{M_{exp}^-}$ | M_{exp}^+ (kN.m) | M_{FE}^+ (kN.m) | $\frac{M_{FE}^+}{M_{exp}^+}$ | Failure mode |
|-------------------|----------------|----------------|---------------|--------------------------|--------------------|------------------|------------------------------|--------------------|-------------------|------------------------------|--------------|
| Ashour et al. [7] | H ₂ | 152.3 | 165.2 | 1.08 | 31.6 | 34.81 | 1.10 | 61.00 | 61.68 | 1.01 | TR |
| | H ₃ | 172.9 | 180.2 | 1.04 | 46.5 | 51.20 | 1.10 | 59.56 | 60.66 | 1.01 | PF |
| | H ₄ | 162.6 | 191.2 | 1.17 | 53.1 | 63.11 | 1.18 | 51.32 | 59.97 | 1.16 | PF |
| | H ₅ | 162.6 | 153.2 | 0.94 | 35.0 | 40.48 | 1.15 | 64.27 | 53.1 | 0.83 | PF |
| | H ₆ | 172.9 | 161.2 | 0.93 | 28.4 | 33.2 | 1.17 | 70.24 | 60.57 | 0.86 | PF |
| | S ₂ | 121.8 | 119.2 | 0.98 | 71.3 | 61.24 | 0.86 | 22.67 | 26.45 | 1.16 | SS |
| | S ₃ | 121.8 | 121.2 | 0.99 | 66.9 | 61.24 | 0.92 | 24.72 | 27.4 | 1.10 | PF* |
| | S ₄ | 170.5 | 166.2 | 0.97 | 89.0 | 74.80 | 0.84 | 37.15 | 42.17 | 1.14 | PF* |
| | S ₅ | 111.7 | 115.2 | 1.03 | 50.2 | 45.19 | 0.90 | 28.36 | 32.55 | 1.14 | SS |

| | | | | | | | | | | | |
|--------------------|----------------|-------|-------|------|------|-------|------|-------|-------|------|-----|
| Subhashree [16] | E ₂ | 178.6 | 175.2 | 0.98 | 79.8 | 75.83 | 0.95 | 45.64 | 45.96 | 1.00 | PF |
| | E ₃ | 207.0 | 223.2 | 1.07 | 53.6 | 48.10 | 0.90 | 72.35 | 82.8 | 1.14 | PF* |
| | E ₄ | 231.4 | 222.2 | 0.96 | 77.0 | 77.78 | 1.01 | 72.29 | 67.48 | 0.93 | PF |
| | E ₅ | 174.6 | 175.2 | 1.0 | 77.4 | 75.75 | 0.98 | 44.87 | 45.99 | 1.02 | PF |
| | SB1 | 320 | 295.2 | 0.93 | - | 35.74 | - | - | 19.03 | - | PF |
| | TB1 | 224 | 223.2 | 0.99 | - | 18.34 | - | - | 18.73 | - | PF |

TR= Tensile rupture of the CFRP sheets over the central support followed by flexural failure, PF= Peeling failure (debonding over the central support), SS=Sheet separation (under concentrated load), PF* = Peeling failure (under concentrated load)

3.2. Comparison of the Load-Deflection Response

This study also performs a comparison between experimentally recorded and numerically simulated applied load-midspan deflection response of reference and FRP-strengthened beams. Only a few database studies contain the applied load-midspan deflection responses of the tested specimens. Here, the results corresponding to the study presented in [7] are shown and described in detail. The geometric properties of the test specimens are shown in Figure 6. and Figure 7. plots the applied load-midspan deflection responses for the reference beam specimen and FRP-strengthened beam specimens. The agreement between numerical simulations and experimental records is excellent for the reference beam and good for the FRP-strengthened beams.

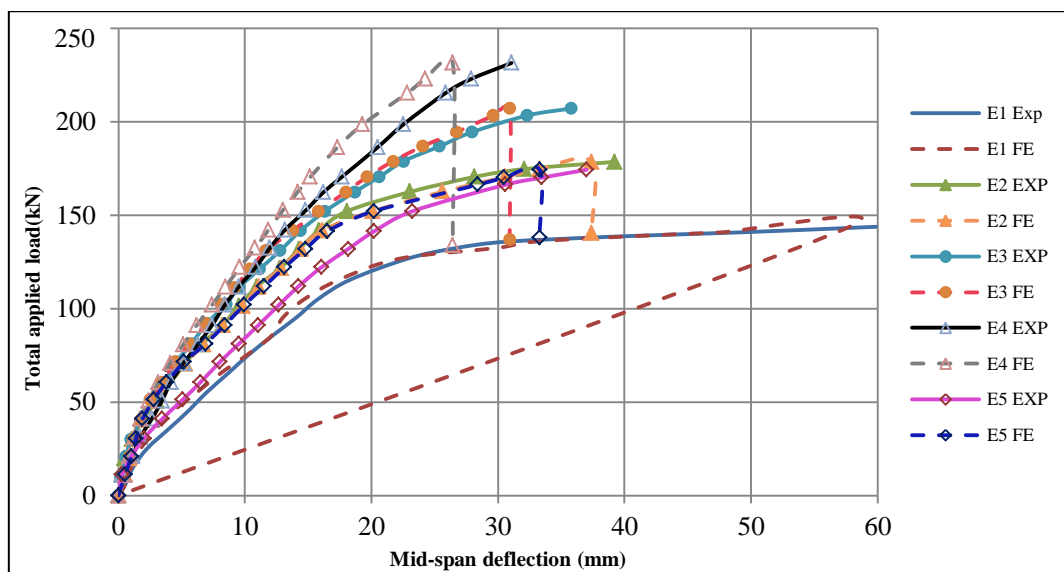


Figure. 7 Comparison between the experimental measurement and FE simulation of the applied force-midspan deflection response for the tests presented in [7]

3.3. Comparison of Hogging and Sagging Bending Moments

Table 3. and Table 4. show that the numerical results of the hogging and the sagging bending moment for the reference beams specimens and FRP-strengthened beams specimens agreed very well with the experimental records.

3.4. Comparison of the Failure Mode

Numerical and experimental records showed that the reference beam failed in a ductile manner because of concrete crushing after large deformations, while the other four strengthened beams failed as a result of a peeling failure (debonding over the central support) of the external CFRP reinforcement.

Figure 8. shows the interfacial shear stress along the adhesive layer of the upper FRP plate of beam E2 at different loads until failure. At a total load of 130.20 kN (before cracking), there is no peeling failure, and the shear stress in FRP is lower than its maximum strength p^T_{max} (3.0 MPa). After the cracking load (155.20 kN), the shear stress in FRP increased significantly until failure (178.20 kN). Figure 8. shows that peeling started at the central support, where maximum stresses are concentrated at the load (170.2 kN) and then propagated to the beam end. Additionally, Figure 9. shows that the normal stress does not exceed the maximum strength p^N_{max} .

Figure 10. shows the interfacial shear stress along the adhesive layer of the lower FRP plate of beam E3 at different loads until failure.

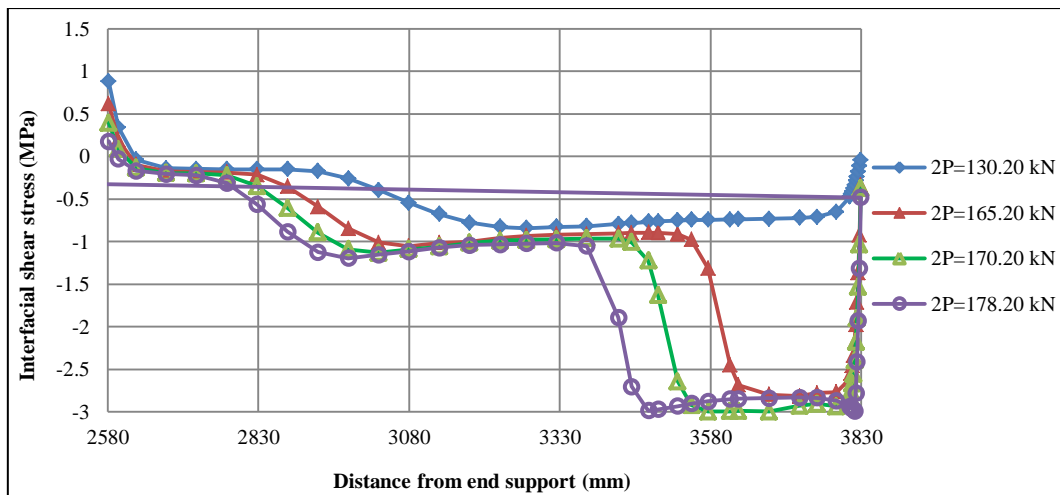


Figure 8. Interfacial shear stress of the adhesive layer of the upper FRP plate of beam E2 at different loads until failure

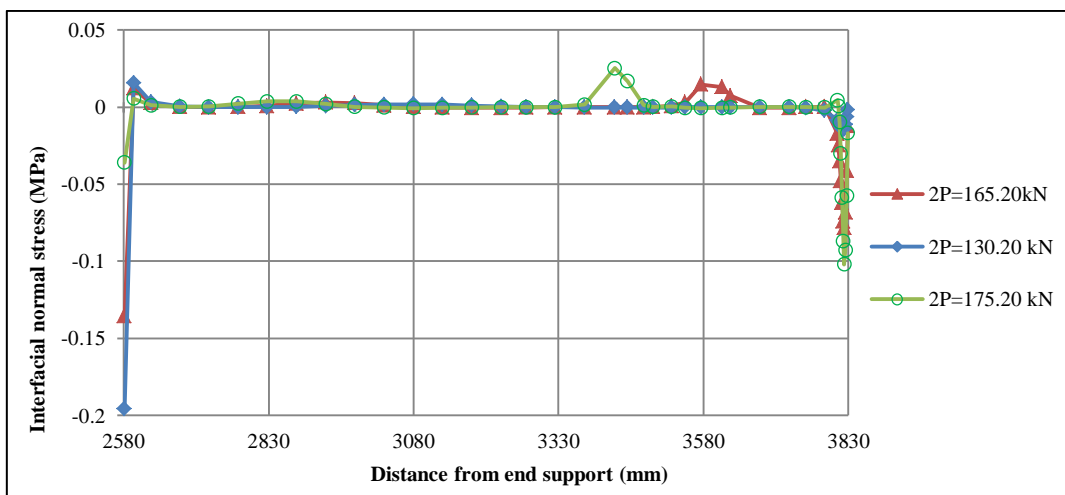


Figure 9. Interfacial normal stress of the adhesive layer of the upper FRP plate of beam E2 at different loads at the plate end

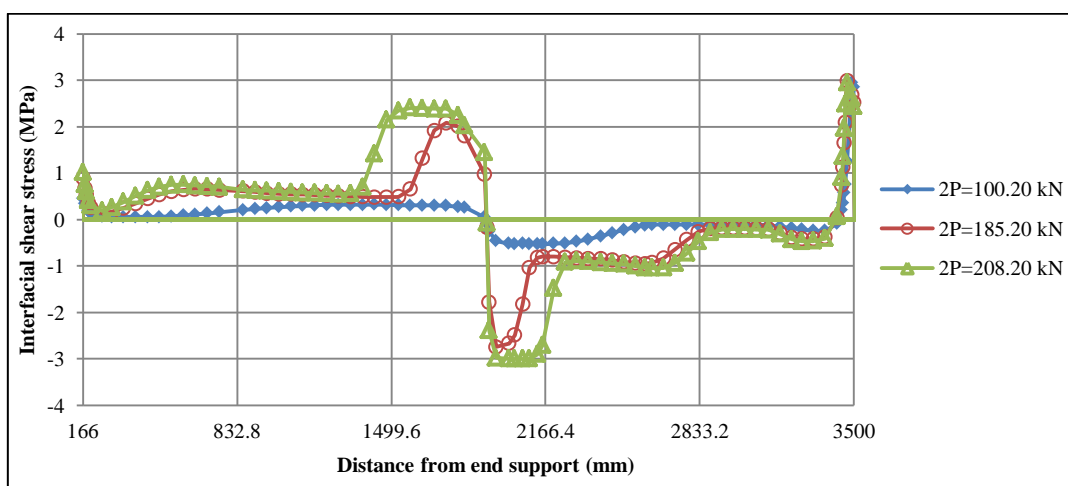


Figure 10. Interfacial shear stress of the adhesive layer of the lower FRP plate of beam E3 at different loads until failure

Additionally, Figures 11. and 12. shows that the normal stress along beam E3 does not exceed its maximum strength p^N_{max} .

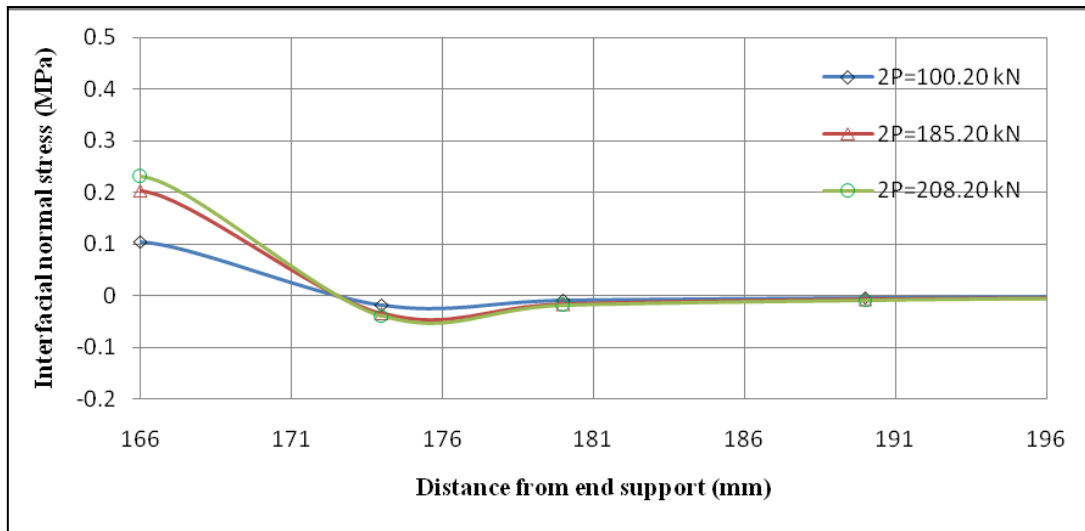


Figure 11. Interfacial normal stress of the adhesive layer of the lower FRP plate of beam E3 at different loads at the plate end

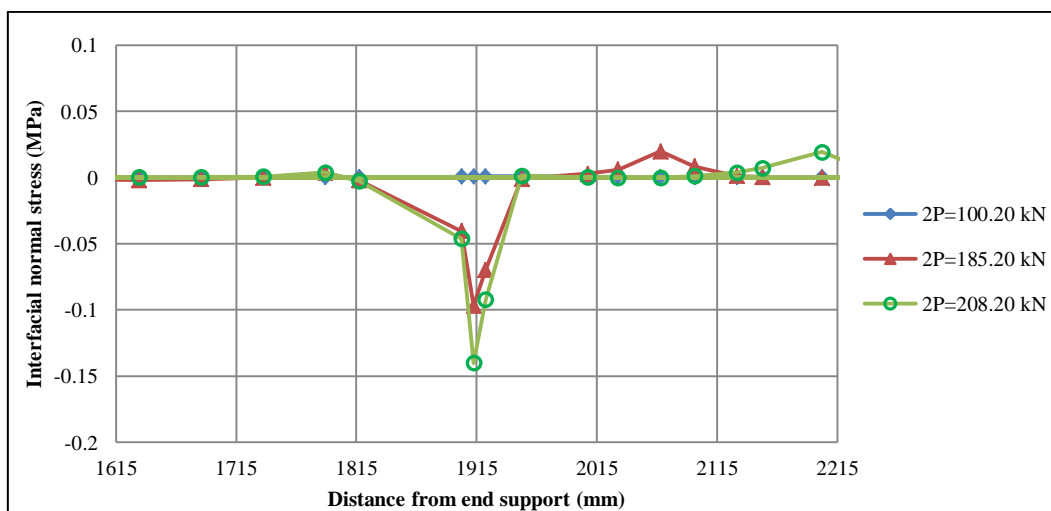


Figure 12. Interfacial normal stress of the adhesive layer of the lower FRP plate of beam E3 at different loads at the concentrated load

4. Effect of Adhesive Fracture Energy on Moment Redistribution

To study the effect of adhesive fracture energy on moment redistribution, four FRP-strengthened RC symmetrical continuous beams with different adhesive fracture energies, in addition to a reference beam, were analysed. Properties of the concrete, steel reinforcement and CFRP plate used in this study are similar to those of beam E4 in [7]. The results of the FE model were tabulated as shown in Table 5.

Figure 13. indicates that it easy to redistribute the moment ($\frac{M_u^-}{M_u^+}$), as in CB, by increasing the adhesive fracture energy. Table 5. shows that $\frac{M_u^-}{M_u^+}$ for beam G₃ is equal to 0.90, the same as CB, which means that the high fracture energy improves the ductility of the strengthened beams.

Figure 14. shows actual and elastic bending moments at failure for the CB, G₀, G₁, G₂, and G₃ beams. The moment redistribution ratios ($\frac{M_{elastic} - M_{failure}}{M_{elastic}}$) at the central support for the CB, G₀, G₁, G₂, and G₃ beams are 16.90%, 11.41%, 10.03%, 9.17%, and 17.20%, respectively. The observed results conclude that, by increasing the adhesive fracture energy of FRP-RC continuous beams, the bending moment can be redistributed, as in CB, and the redistributed bending moment ratios of CB and the beam G₃ are very close; as mentioned above.

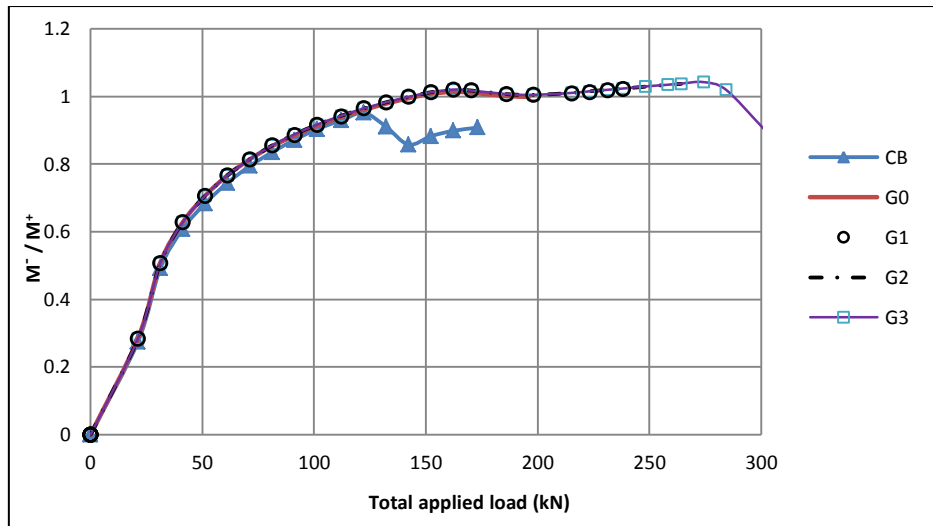


Figure 13. Comparison between the FE simulation of the applied load-hogging /-sagging moment ratio responses for the CB, G0, G1, G2 and G3 beams

Table 5. Numerical results of the load-carrying capacity, ultimate negative and positive moment at failure and failure mode of the FRP-strengthened RC beams at different adhesive fracture energies

| ID | G _I MN/m | G _{II} MN/m | M _u ⁻ (kN.m) | M _u ⁺ (kN.m) | M _u ⁻ / M _u ⁺ |
|----------------|------------------------|-------------------------|---------------------------------------|---------------------------------------|--|
| CB | - | - | 51.82 | 57.00 | 0.91 |
| G ₀ | 0 | 0 | 62.58 | 62.64 | 1.00 |
| G ₁ | 0.00007 | 0.0002 | 77.48 | 75.77 | 1.02 |
| G ₂ | 0.0001 | 0.0009 | 86.40 | 83.28 | 1.04 |
| G ₃ | 0.001 | .009 | 89.78 | 99.31 | 0.90 |

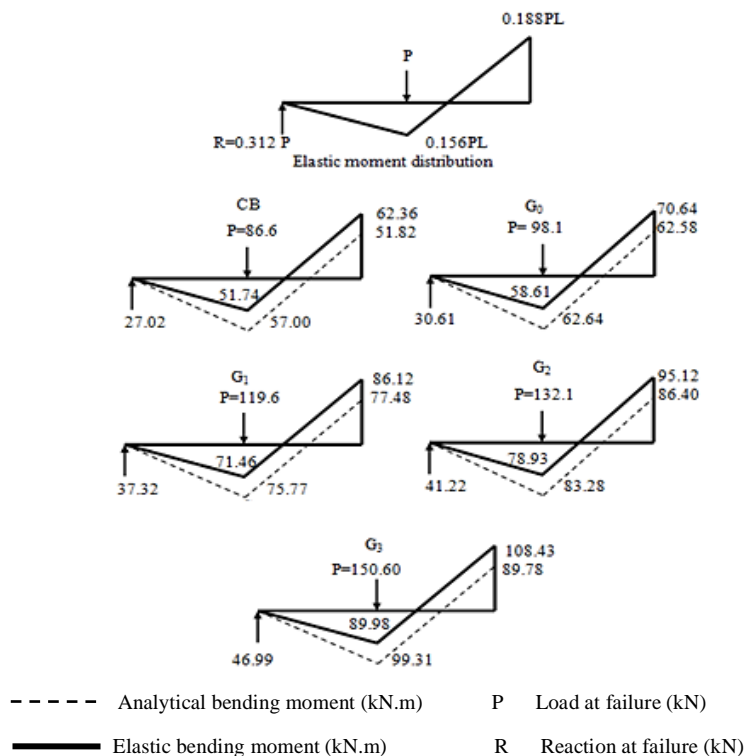


Figure 14. Actual versus elastic bending moment at failure

5. Conclusions

- A simple and efficient uniaxial nonlinear finite-element model that can accurately estimate the ultimate load and the behaviour of reinforced concrete (RC) continuous beams flexurally strengthened with externally bonded FRP plates on the upper and lower fibres is presented in this paper. A twenty one- degree- of- freedom element is suggested with layer-discretization of the cross-sections of the RC beam for FE modelling. Realistic nonlinear constitutive relations are employed to describe the stress-strain behaviour of each component of the strengthened beam. The FE model is based on nonlinear fracture mechanics. The uniaxial nonlinear finite-element model is able to model different experimentally observed failure modes, i.e., collapse due to concrete crushing, reinforcing steel yielding, FRP rupture, plate end interfacial debonding, concrete cover separation at the plate ends, and intermediate crack induced interfacial debonding.
- Results of the proposed FE model are verified by comparing them with experimental measurements available in the literature. The numerical results of the plated beams (beams strengthened with FRP plates) agreed very well with the experimental results. In addition, the uniaxial nonlinear finite-element model results provided good predictions of the specific failure modes obtained from tests.
- Shear stresses, where maximum loads are concentrated and at the central support, demonstrate the failure mode, while normal stresses have a small effect.
- The bending moment of FRP-RC continuous beams can be redistributed as in control beams when the adhesive fracture energy is considered.

6. References

- [1] ACI 440, Guide for the design and construction of externally bonded FRP systems for strengthening concrete structures. Technical Report, American Concrete Institute. 2011.
- [2] CEB-FIB Model Code 90, Thomas Telford Eds., London, 1993.
- [3] JSCE, Recommendations for upgrading of concrete structures with use of continuous fiber sheets. Technical Report, Research Committee on Upgrading of Concrete Structures with Use of Continuous Fiber Sheets, Japanese Society of Civil Engineers, 2000.
- [4] Grace NF, Sayed GA, Soliman AK, Saleh KR. Strengthening Reinforced Concrete Beams Using Fiber Reinforced Polymer (FRP) Laminates. *ACI Structural Journal* 1999. p. 865-875.
- [5] Grace NF. Strengthening of negative moment region of RC beams using CFRP strips. *ACI Structural Journal* 2001; 3(98):347-358.
- [6] El-Refaie SA, Ashour, AF and Garrity SW. CFRP strengthened continuous concrete beams. in *Proceedings of the Institution of Civil Engineers. Structures and buildings* 2003; 156(4):395-404.
- [7] Ashour, AF, El-Refaie SA and Garrity SW. Flexural strengthening of RC continuous beams using CFRP laminates. *Cement and Concrete Composite J* 2004; 26(7):765-775.
- [8] Maghsoudi AA, Bengar H. Moment redistribution and ductility of RHSC continuous beams strengthened with CFRP. *Turkish Journal of Engineering and Environmental Sciences* 2009; 33:45-59.
- [9] Rahman M., Jumaat M. The Effect of CFRP laminates length for strengthening the tension zone of the reinforced concrete T-beam. *Journal of scientific research & reports* 2013; 2(2):626-640.
- [10] Aiello MA, Valente L, Rizzo A. Moment redistribution in continuous reinforced concrete beams strengthened with carbon-fiber-reinforced polymer laminates. *Mechanics of composite materials* 2007; 43(5):453-466.
- [11] Deifalla, A., Awad, A., and Elgarhy, M. "Effectiveness of externally bonded CFRP strips for strengthening flanged beams under torsion: An experimental study." *Journal of Engineering Structures*, 2013; 56: 2065-2075.
- [12] Kotynia, R.; Cholostiakow, S. New proposal for flexural strengthening of reinforced concrete beams using CFRP T-shaped profiles. *Polymers* 2015, 7, 2461-2477.
- [13] Rahman, M.; Jumaat, M.Z.; Rahman, M.A.; Qeshta, I.M.I. Innovative hybrid bonding method for strengthening reinforced concrete beam in flexure. *Constr. Build. Mater.* 2015, 79, 370-378.
- [14] Elwan SK. Torsion strengthening of RC beams using CFRP (Parametric Study). *KSCE Journal of Civil Engineering*. 2016:1-9.
- [15] Fakhreddine D, Youcef G, Yazid A, Li A. Strengthening in flexure-shear of RC beams with hybrid FRP systems: Experiments and numerical modeling. *Journal of Reinforced Plastics & Composites*. 2016: 17-25

- [16] Subhashree S. Strengthening of RC continuous beam using FRP sheet. Master Thesis No. 210CE2032, Department of Civil Engineering, National Institute of Technology Rourkela, Odisha, India, 2012.
- [17] Jerome DM, Ross CA. Simulation of the dynamic response of concrete beams externally reinforced with carbon-fiber reinforced plastic. *Computers and Structures*, 1997; 64(5):1129–1153.
- [18] Moller B, Graf W, Hoffmann A, Steinigen F. Numerical simulation of RC structures with textile reinforcement. *Computers and Structures* 2005; 83:1659–1688.
- [19] Camata G, Spacone E, Zarnic R. Experimental and nonlinear finite element studies of RC beams strengthened with FRP plates. *Composites* 2007; 38:277–288.
- [20] Zhang L, Teng JG. Finite element prediction of interfacial stresses in structural members bonded with a thin plate. *Engineering Structures* 2010; 32:459–471.
- [21] Kotynia R, Baky HA, Neale KW, Ebead UA. Flexural strengthening of RC beams with externally bonded CFRP systems: test results and 3D nonlinear FE analysis. *Journal of Composite Construction ASCE* 2008; 12(2):190–201.
- [22] Obaidat YT, Heyden S, Dahlblom O. The effect of CFRP and CFRP/concrete interface model when modelling retrofitted RC beams with FEM. *Computers and Structures* 2010;92:1391–1398.
- [23] Barbato M. Efficient finite element modeling of reinforced concrete beams retrofitted with fibre reinforced polymers. *Computers and Structures* 2009; 87:167–176.
- [24] Sakr MA. FE modeling of simply supported RC beams strengthened with FRP plates. 13th International conference on structural faults and repair, Edinburgh, UK, 2010.
- [25] Mander JB, Priestley MJN, Park R. Theoretical stress-strain model for confined concrete. *Journal of Structural Engineering (ASCE)* 1998; 114(8):1804–1826.
- [26] Stevens NJ, Uzumeri SM, Collins MP, Will GT. Constitutive model for reinforced concrete finite element analysis. *ACI Structural Journal* 1991; 88(1):49-59.
- [27] Fragiaco M, Amadio C, Macorini L. Finite-element model for collapse and long-term analysis of steel-concrete composite beams. *Struct. Eng., ASCE* 2004; 130(3):489–497.
- [28] Kafkalidis MS, Thouless MD. The effects of geometry and material properties on the fracture of single lap-shear joints. *International Journal of Solids and Structures* 2002; 39:4367–4383.
- [29] Li S, Thouless MD, Waas AM, Schroeder JA, Zavattieri PD. Mixed-mode cohesive-zone models for fracture of an adhesively bonded polymer-matrix composite. *Engineering Fracture Mechanics* 2006; 73:64–78.
- [30] Tvergaard V. Effect of fiber debonding in a whisker-reinforced metal. *Material Science and Engineering* 1990; 125:203–213.
- [31] Högberg JL. Mixed mode cohesive law. *International journal of Fracture* 2006; 141:549–559.
- [32] Guo ZG, Cao SY, Sun WM, Lin XY. Experimental study on bond stress-slip behaviour between FRP sheets and concrete. In: FRP in construction, proceedings of the international symposium on bond behaviour of FRP in structures 2005:77–84.